Crystallization Kinetics and Crystallization-Induced Morphological Formation in the Blends of Poly(ϵ-caprolactone)-*block*-polybutadiene and Polybutadiene Homopolymer

Jen-Yung Hsu,[†] I-Fan Hsieh,[†] Bhanu Nandan,[†] Fang-Choyu Chiu,[‡] Jean-Hong Chen,[§] U-Ser Jeng,[⊥] and Hsin-Lung Chen*,[†]

Department of Chemical Engineering, National Tsing Hua University, Hsin-Chu 30013, Taiwan; Department of Chemical and Materials Engineering, Chang Gung University, Kwei-San, Taoyuan 333, Taiwan; Department of Polymer Materials, Kun Shan University, Yung-Kang City, Tainan Hsien 71003, Taiwan; and National Synchrotron Radiation Research Center, Hsin-Chu 300, Taiwan R.O.C.

Received February 12, 2007; Revised Manuscript Received April 25, 2007

ABSTRACT: The crystallization kinetics and the perturbation of the melt mesophase induced by crystallization in the blends of a symmetric poly(ϵ-caprolactone)-*block*-poly(1,4-butadiene) (PCL-*b*-PB) and a poly(1,4-butadiene) homopolymer (h-PB) have been investigated. The crystallization at low to moderate undercooling was found to break out the melt structure and transformed it into a crystalline lamellar structure. The mechanism of the morphological breakout in a cylinder-forming blend with the overall volume fraction of PB (f_{PB}) of 0.78 was resolved by time-resolved simultaneous small-angle X-ray scattering (SAXS) and wide-angle X-ray scattering (WAXS). The results revealed two steps involved in the breakout process. At the initial stage of crystallization, the formation of crystallites within a portion of PCL cylinders deformed the microdomains and initiated local coalescence of the domains through conformational communication of the coronal PB blocks. After this stage the crystallinity started to develop rapidly, and the crystallization was proposed to occur via diffusion of PCL blocks to the crystal growth front, which then induced the formation of extended lamellar morphology. The isothermal crystallization kinetics of the cylinder-forming blend with $f_{PB} = 0.74$ was also studied. Interestingly, the overall crystallization rate exhibited an abrupt increase at very large undercooling ($\Delta T \simeq 96$ K). This anomalous acceleration of crystallization rate indicated that the crystallization kinetics was largely controlled by homogeneous nucleation when the morphological breakout was strongly restricted at very low temperatures.

Introduction

Microphase separation of diblock copolymer and its blend with the corresponding homopolymer in the melt state may generate a series of long-range ordered microdomains, including lamellae, cylinder, and sphere.[1−5] In crystalline−amorphous (C−A) diblock copolymers, the structural formation becomes more complex as the crystallization driving force may perturb the melt mesophase formed by microphase separation. According to the extent of structure perturbation, the crystallization of C−A diblocks has been classified into three modes, namely, confined, templated, and breakout.[6,7] Confined crystallization is defined as the case where the crystallization is totally restricted within the individual microdomains.[8] Breakout crystallization corresponds to the other extreme where crystallization is able to disrupt the melt mesophase and transforms it into an extended crystalline lamellar morphology.[9−12] Templated crystallization represents an intermediate regime where the crystallization induces local welding of microdomains through short-range intrusion of the crystal growth front into the nearby domains.[6,13]

Recent studies have revealed that the ability of the crystallization to perturb the melt morphology of C−A diblocks is governed by the T_g of the A block,[14−17] microdomain geometry, and the strength of interblock repulsion.[6,7] In the case of the blend system, homopolymer A (h-A) solubilized in A domains also plays a crucial role, as has been demonstrated for the sphere-forming blends of poly(ethylene oxide)-*block*-poly(1,4-butadiene) (PEO-*b*-PB) and h-PB.[18,19] In neat PEO-*b*-PB, the tendency of PEO crystallization in spherical microdomains to transform the melt structure to the lamellar morphology was overwhelmed by the driving force of microphase separation since the segregation strength between PEO and PB was strong; therefore, only local coalescence of several spheres occurred. The microdomain coalescence was completely suppressed in the sphere-forming blend, indicating that the presence of h-PB tended to hinder the morphological breakout.

In this study, we center on a relatively weakly segregated system, poly(ϵ-carprolactone)-*block*-polybutadiene (PCL-*b*-PB), which is expected to undergo more drastic morphological perturbation during PCL crystallization compared with the PEO-*b*-PB system. Nojima et al.[9−12] have found that the crystallization of PCL blocks in neat PCL-*b*-PB always led to a crystalline lamellar morphology even when PCL blocks were prerestricted in the spherical microdomains in the melt. Such a breakout process was also found to occur quite rapidly (say, less than 5 min at room temperature) irrespective of the microdomain morphology. In the present study, we intend to examine the crystallization mode in the wet-brush blends of PCL-*b*-PB with h-PB to reveal the role of homopolymer for the system in which the crystallization driving force may overwhelm the driving force of microphase separation prescribed by the segregation strength. Here we blend a symmetric PCL-*b*-PB with a low-molecular-weight h-PB to form a series of blends with different overall PB volume fraction (f_{PB}) to demonstrate that the large-scale morphological breakout, although it may still take place

* To whom correspondence should be addressed. E-mail: hslchen@mx.nthu.edu.tw.
[†] National Tsing Hua University.
[‡] Chang Gung University.
[§] Kun Shan University.
[⊥] National Synchrotron Radiation Research Center.

10.1021/ma070369+ CCC: $37.00
Published on Web 06/07/2007

under certain conditions, is retarded significantly by the existence of h-PB. Using this system, we are able to monitor the breakout process in situ by means of simultaneous time-resolved SAXS/WAXS experiments, such that the mechanism associated with the transformation from the initial melt structure to the final crystalline lamellar structure may be elucidated. We will show that a phase separation between h-PB and PB blocks occurs at low level of crystallinity due to local coalescence of PCL microdomains. A rapid development of crystallinity then sets in and transforms the morphology into an extended crystalline lamellar structure. Finally, we will present the kinetics of both nonisothermal and isothermal crystallizations of a cylinder-forming PCL-*b*-PB/h-PB blend. It will be shown that this composition exhibits an anomalous temperature dependence of the overall crystallization rate, where the crystallization kinetics shows an upturn at very low crystallization temperature (T_c). This anomalous acceleration of crystallization rate is attributed to the dominance of homogeneous nucleation in controlling the overall crystallization kinetics at very large undercooling where the breakout process is greatly restricted.

Experimental Section

Materials. The PCL-*b*-PB with the polydispersity index (M_w/M_n) of 1.08 was synthesized by sequential anionic polymerization (Polymer Source, Inc.). The M_n of PCL block ($M_{b,PCL}$) was 12.5×10^3 and M_n of PB block ($M_{b,PB}$) was 11.5×10^3, prescribing $f_{PB} = 0.52$. The 1,4-addition PB homopolymer with $M_n = 2.3 \times 10^3$ was also synthesized by anionic polymerization (Polymer Source, Inc.). The blends with f_{PB} of 0.64, 0.74, 0.78, 0.83, and 0.87 were prepared by solvent-casting. PCL-*b*-PB and h-PB were first dissolved in tetrahydrofuran at room temperature (ca. 27 °C). The microphase-separated blend was obtained by removing most of the solvent on a hot plate at 80 °C, followed by drying in vacuo at 60 °C for 2 h for complete removal of residual solvent.

X-ray Scattering Measurement. The morphologies in the melt and the crystalline state were detected by the in-house SAXS. The SAXS instrument was equipped with an 1.3 KW X-ray generator operated at 40 kV × 35 mA (NANOSTAR, Bruker Co, Ltd.) and a two-dimensional position-sensitive proportional counter. The Cu Kα line ($\lambda = 0.154$ nm) was used. The intensity profile was output as the plot of the scattering intensity (I) vs the scattering vector, $q = (4\pi/\lambda)\sin(\theta/2)$ (θ = scattering angle). The SAXS profiles were corrected for the absorption, the air scattering, and the background arising from thermal diffuse scattering (TDS). The intensity level of TDS was assumed to be a constant over the q range covered in this study, and its magnitude was determined from the slope of the Iq^4 vs q^4 plot at the high-q region ($q > 1.3$ nm^{-1}).

Simultaneous SAXS/WAXS experiments were conducted in the National Synchrotron Radiation Research Center (NSRRC), Taiwan. The X-ray beam, monochromated to 1.2 Å in wavelength, was collimated into a beam size of 0.5 mm in height and 0.5 mm in width. A two-dimensional multiwired area detector was used to record the scattering intensity. The sample was first annealed at 85 °C for 3 min followed by rapidly quenched to 26 °C for isothermal crystallization. The time-resolved SAXS/WAXS data were collected for 5 min for each frame. The synchrotron X-ray scattering results presented here have also been corrected for background, detector sensitivity, incident beam intensity, and TDS.

Real-Space Morphological Observation. The real-space morphologies of the blends were observed by a JEOL JEM-2000FXZ transmission electron microscope (TEM) operated at 100 kV. The film specimens were microtomed at −90 °C using a Reichert Ultracut E low-temperature sectioning system. The ultrathin sections were picked onto the copper grids coated with carbon-supporting films followed by staining by exposure to the vapor of 2% OsO_4-(aq) for 2 h. Since OsO_4 is a preferential staining agent for PB, PB and PCL domains appear as dark and bright regions in the micrographs, respectively.

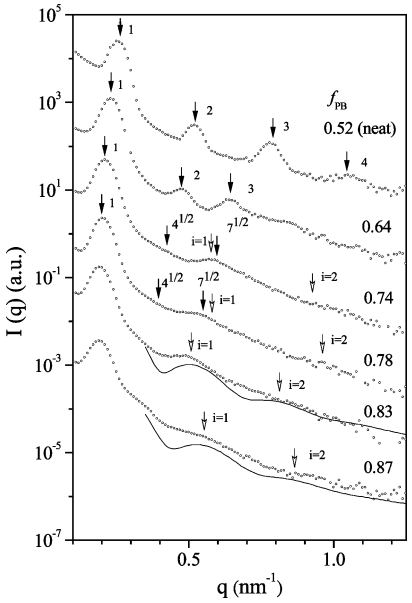

Figure 1. SAXS profiles of neat PCL-*b*-PB and PCL-*b*-PB/h-PB in the melt. The experiments were conducted at 85 °C. The lattice peaks are marked by solid arrows whereas opened arrows indicate the form factor peaks associated with the scattering from individual microdomains. The solid curves are the profiles calculated using theoretical spherical form factor with the average radius of 10.5 nm for the blend with $f_{PB} = 0.83$ and of 10.8 nm for that with $f_{PB} = 0.87$. Gaussian distributions were assumed for the radius.

Crystallization Kinetics Study. The crystallization kinetics of PCL blocks in the blends were studied for both nonisothermal and isothermal conditions by a TA Instruments 2000 differential scanning calorimeter (DSC). For nonisothermal crystallization experiments, the samples were first annealed at 85 °C for 5 min and then cooled to −80 °C at 5 °C/min for recording the crystallization exotherm. The temperature corresponding to the exothermic peak was denoted as T_f. For isothermal crystallization experiments, the samples were first annealed at 85 °C for 5 min on a Linkam HFS 91 hot stage followed by transferring into the DSC equilibrated at the desired T_cs at which the isothermal crystallizations were conducted.

Results and Discussion

Melt and Crystalline Morphology. The morphologies of PCL-*b*-PB/h-PB blends in the melt state are probed by SAXS at 85 °C, which lies above the melting point of PCL. As shown in Figure 1, neat PCL-*b*-PB and the blend with $f_{PB} = 0.64$ show well-defined lattice peaks with relative positions (i.e., 1:2:3:4) relevant to lamellar morphology. The interlamellar distance calculated from the primary peak position (q_m) via $L = 2\pi/q_m$ of neat PCL-*b*-PB is 24.9 nm. The thickness of PCL lamellae ($L_{PCL} = Lf_{PCL}$) is hence 11.0 nm. The scattering profiles of the blends with $f_{PB} = 0.74$ and 0.78 display lattice peaks with the relative positions ($1:4^{1/2}:7^{1/2}$) relevant to hexagonally packed cylinder morphology. The $7^{1/2}$ peak overlaps with the first form factor peak (marked by "$i = 1$") of the PCL cylinders. The positions of the form factor maxima prescribe the radius (R) of 9.0 and 8.8 nm for the cylinders in the blend with $f_{PB} = 0.74$ and $f_{PB} = 0.78$, respectively. The calculated f_{PB}s using the values of R and the interdomain distances deduced from the primary peak positions with the assumption of hexagonal lattice are 0.75 and 0.78, respectively, which agree well with the values prescribed by the overall blend compositions.

The SAXS profiles of the blends with $f_{PB} = 0.83$ and 0.87 show a rather broad primary peak without obvious higher-order peaks, suggesting that the PCL domains do not arrange in long-

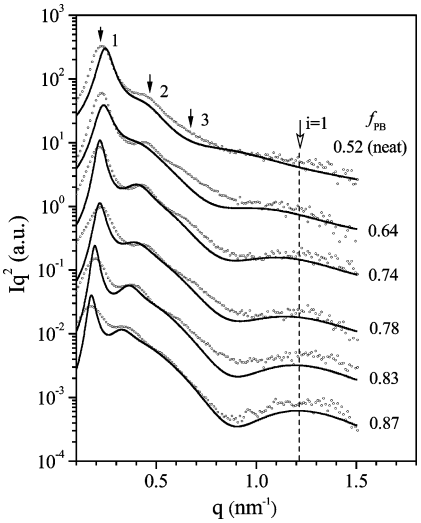

Figure 2. Lorentz-corrected SAXS profiles of neat PCL-*b*-PB and PCL-*b*-PB/h-PB crystallized at 26 °C for 48 h. The lattice peaks are marked by solid arrows whereas opened arrows indicate form factor peaks associated with the scattering from individual lamellae. The solid curves represent the fits by eq 1.

range ordered lattice. The first form factor peaks are however visible. The form factor profiles can be fitted by the spherical form factor with the assumption of Gaussian distribution of radius[20] (cf. the solid curves). The average radius obtained from the fitting is 10.5 and 10.8 nm for the blend with $f_{PB} = 0.83$ and 0.85, respectively. The analysis of the SAXS profiles in Figure 1 concludes that a series of microdomain morphology can be accessed by blending a lamellae-forming PCL-*b*-PB with h-PB. Neat PCL-*b*-PB and the blend with $f_{PB} = 0.64$ exhibit lamellar morphology in the melt. The PCL blocks in the blends with $f_{PB} = 0.74$ and 0.78 form cylindrical domains, while those in the blends with $f_{PB} = 0.83$ and 0.87 form spherical domains.

Figure 2 shows the Lorentz-corrected SAXS profiles of the blends after crystallization at 26 °C for 48 h to examine the effect of crystallization on the melt morphology. It can be seen that all the scattering profiles display lattice peaks with the relative positions of 1:2:3, showing that a lamellar morphology with alternating PCL and PB layers forms after the crystallization irrespective of the melt structure. In this case, the crystallization can break out the cylindrical and spherical microdomains in the melt. The broad peak at around 1.25 nm^{-1} is attributed to the first form factor peak of the PCL crystalline lamellae. The thickness of the lamellae estimated from this peak position via $L_{PCL} = 9.8/q_m^{i=1}$ is 7.8 nm.[21] The position of this form factor peak is almost the same for all samples, implying similar PCL lamellar thickness in the system regardless of f_{PB}.

The observed SAXS profiles are further fitted by the following scattering function based on a lamellar stacking model with Gaussian distributions of the layer thicknesses.[21]

$$Iq^2 \propto \frac{1}{q^2}\frac{1}{(1-g_ag_b)^2 + 4g_ag_b\sin^2(qL/2)}[(1-g_a)(1-g_b) \times (1-g_ag_b) + 2g_a(1-g_b)\sin^2(qL_a/2) + 2g_b(1-g_a) \times \sin^2(qL_b/2)] \quad (1)$$

$$g_a = \mathrm{e}^{-(1/2)\sigma_a^2q^2} \quad (2)$$

$$g_b = \mathrm{e}^{-(1/2)\sigma_b^2q^2} \quad (3)$$

where L_i is the thickness of layer i ($i = a$ or b with a standing for PCL and b standing for PB) and σ_i is the standard deviation of the layer thickness. The fitted results are displayed by the solid curves in Figure 2, and the morphological parameters obtained from the fits can be found in the Supporting Information. The comparison between the interlamellar distance obtained from the fitting and that calculated by the overall PCL composition ($L' = L_{PCL}/f_{PCL}$ with L_{PCL} determined from the fit) is shown in Figure 3. L' corresponds to the interlamellar distance if all h-PB remains within the PB lamellar domains after PCL crystallization. It can be seen that L is slightly larger than L' at $f_{PB} < 0.74$; by contrast, at $f_{PB} \geq 0.74$ L' becomes obviously larger than observed L. This means that a fraction of h-PB is expelled out of the PB lamellar domains during PCL crystallization, such that the PB blocks attached to the PCL lamellae accommodate less h-PB than those in the corresponding melt state.

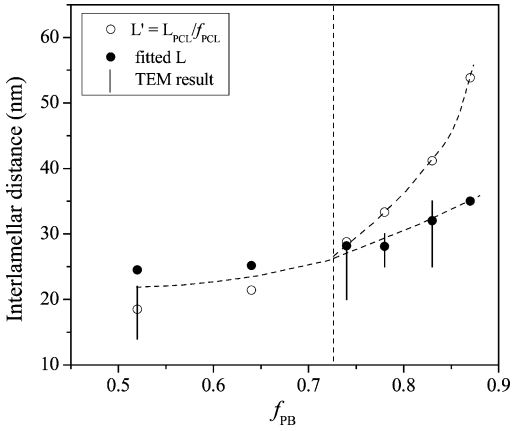

Figure 3. Interlamellar distances as a function of f_{PB} for the samples crystallized at 26 °C for 48 h.

TEM was also conducted to reveal the crystalline morphology in real space. Figure 4 shows the TEM micrographs of the samples with $f_{PB} = 0.52$ (neat), 0.74, and 0.78 after crystallization at 26 °C. The micrographs demonstrate the formation of lamellar morphology in all samples. The thickness of the PCL domains estimated from the micrographs is 6−9 nm, and the corresponding interlamellar distances are also shown in Figure 3 for comparison. It is noted that relatively large PB domains situating between the lamellae stacks are observed for the blend with $f_{PB} = 0.78$. The existence of these domains further attests that a fraction of h-PB is expelled out of the PB lamellar microdomains during PCL crystallization. On basis of the SAXS and TEM studies, we conclude that isothermal crystallization of PCL-*b*-PB/h-PB blends at moderate undercooling is able to disrupt the melt structure and transform it into a lamellar morphology. This morphological breakout is accompanied by the segregation of a portion of h-PB out of PB lamellar domains at $f_{PB} \geq 0.74$.

Mechanism of the Breakout Crystallization. A simultaneous SAXS/WAXS measurement was conducted to reveal the mechanism of the breakout crystallization in a cylinder-forming blend with $f_{PB} = 0.78$. Figure 5 and Figure 6 show the SAXS and WAXS results, respectively, for the crystallization at 26 °C. According to the previous study of a sphere-forming PCL-*b*-PB,[10] the breakout of spherical PCL domains induced by the crystallization at 28.4 °C took place within 5 min. However, for the present cylinder-forming PCL-*b*-PB/h-PB blend, the scattering profile remains essentially unperturbed before 240 min, signaling that the morphological perturbation starts after at least 240 min. This means that the existence of h-PB in the blend does retard the crystallization-induced

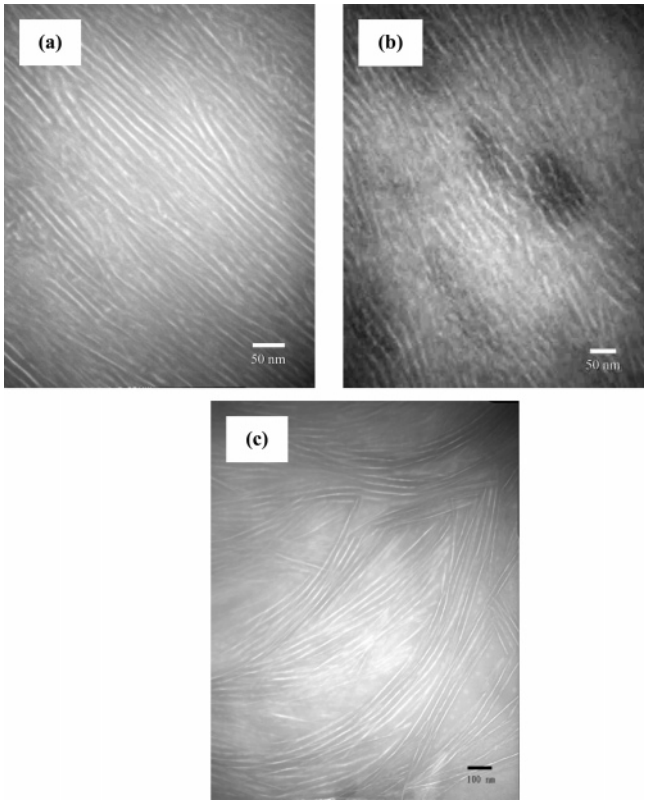

Figure 4. TEM micrographs of PCL-*b*-PB/h-PB with f_{PB} = (a) 0.52 (neat), (b) 0.74, and (c) 0.78 crystallized at 26 °C for 48 h.

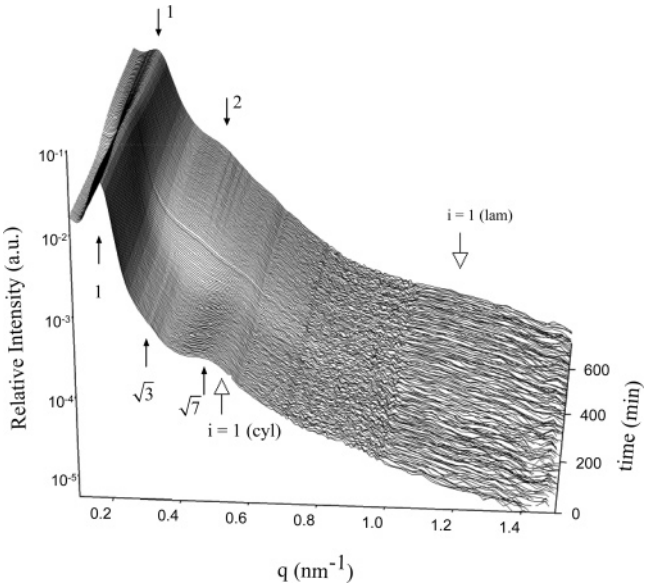

Figure 5. Time-resolved SAXS profiles of PCL-*b*-PB/h-PB with f_{PB} = 0.78 isothermally crystallized at 26 °C.

morphological perturbation, which is consistent with our previous work on PEO-*b*-PB/h-PB blends.[18,19]

Figure 7 displays the temporal development of crystallinity (X_c) obtained from the WAXS profiles. The crystallinity development is characterized by a sigmoidal curve. The crystallinity is very low (<0.05) between 240 and 360 min; however, the corresponding SAXS profiles exhibit obvious change during this period. It can be seen from Figure 5 that the cylinder form factor peak at $q \sim 0.5$ nm^{-1} (marked by "$i = 1$ (cyl)") is significantly smeared at $t = 330$ min, signaling that the structure of a significant portion of PCL cylinders is perturbed despite of very low crystallinity in the system. The structural perturbation within this time period is revealed by TEM. In this experiment, the blend was microtomed at −90 °C, and the ultrathin section on the copper grid was annealed at 85 °C for 3 min followed by isothermal crystallization at 26 °C for 1.5 and 24 h. The reason why the specimen was annealed at 85 °C is to eliminate the crystallinity developed during the micortoming. After the crystallization at 26 °C for the desired time, the specimen was immediately stained by OsO_4 vapor to preserve the morphology developed during the crystallization. The specimen having been crystallized for 1.5 h corresponds to the sample with tiny crystallinity, while the one having been crystallized for 24 h should have reached the ultimate level of crystallinity.

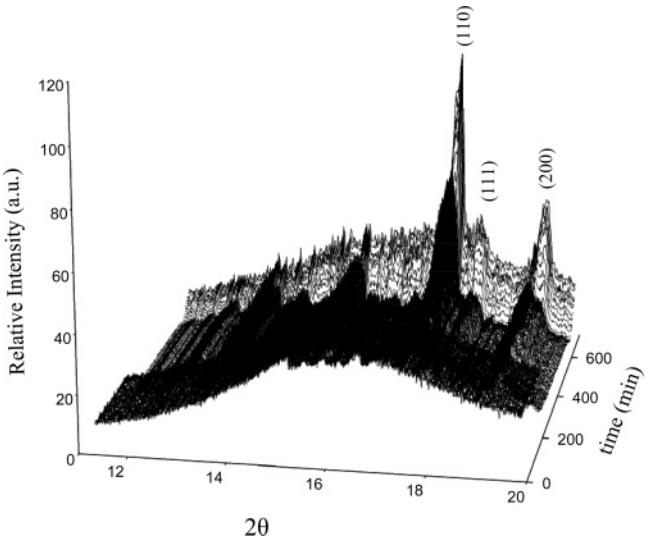

Figure 6. Time-resolved WAXS profiles of PCL-*b*-PB/h-PB with f_{PB} = 0.78 isothermally crystallized at 26 °C.

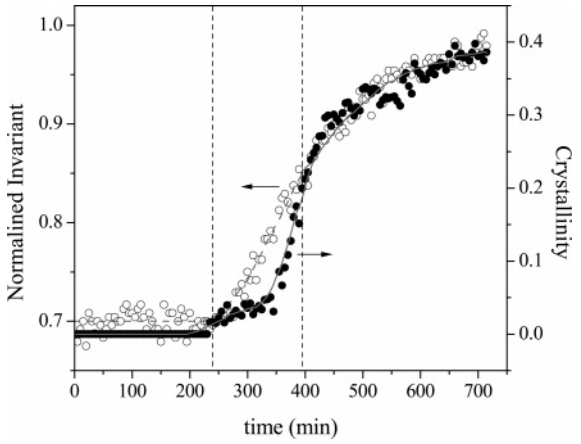

Figure 7. Crystallinity and normalized invariant as a function of time for PCL-*b*-PB/h-PB with f_{PB} = 0.78 isothermally crystallized at 26 °C. The solid curve corresponds to the invariant calculated using eq 8.

Figure 8a displays the TEM micrograph of the sample stained by OsO_4 right after annealing at 85 °C. The melt annealing induces a strong orientation of the PCL cylinders as nearly all cylindrical microdomains are found to show edge-on arrangement. Coalescence of some PCL cylinders is observed after crystallization for 1.5 h, giving rise to the rather tortuous striation image in Figure 8b. It is noted that these striations should not correspond to the side view of PCL cylinders because the cylindrical domains after the melt annealing arrange in a highly ordered hexagonal lattice; in this case, the side view of these cylinders should appear as regular arrays of straight striations rather than the tortuous striations observed in Figure 8b.

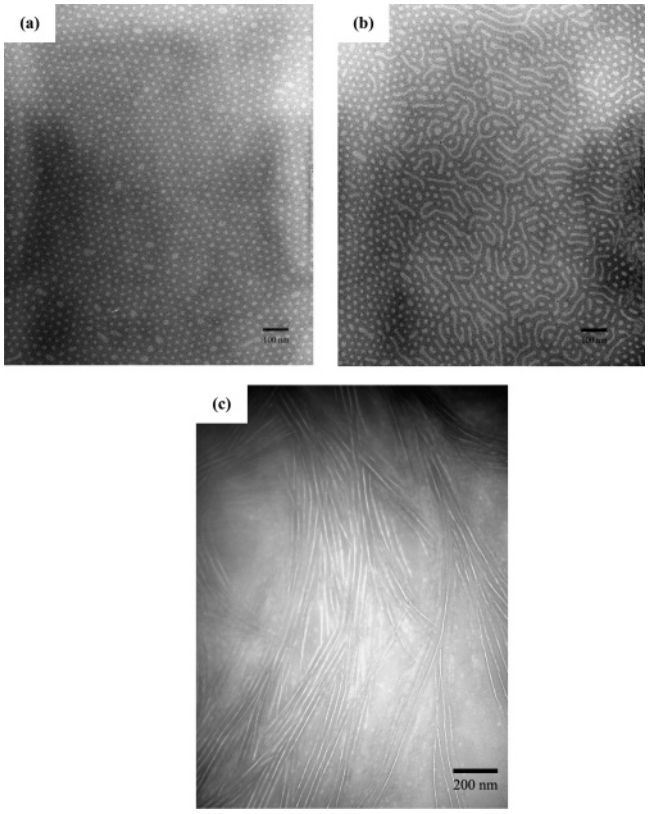

Figure 8. TEM micrographs of PCL-*b*-PB/h-PB with $f_{PB} = 0.78$ isothermally crystallizatized at 26 °C for (a) 0, (b) 1.5, and (c) 24 h followed by staining with OsO_4.

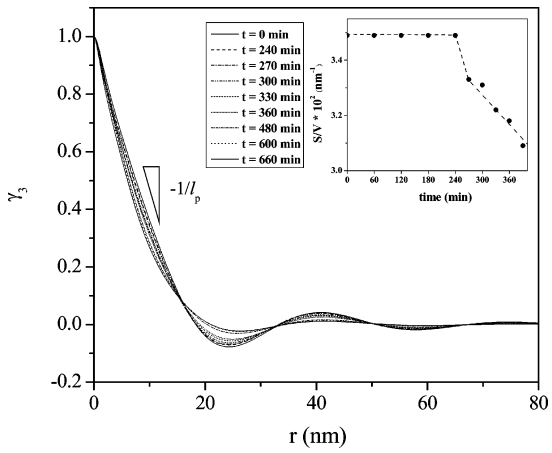

Figure 9. 3-D correlation functions of PCL-*b*-PB/h-PB with $f_{PB} = 0.78$ obtained from the SAXS curves in Figure 5. The inset shows the *S*/*V* as a function of time obtained from the 3-D correlation function.

The image of the coalesced domains is apparently different from that of the crystalline lamellae observed after 24 h of crystallization shown in Figure 8c. Moreover, the thickness of the coalesced domains (ca. 13−20 nm) is thicker than that of the PCL crystalline lamellae (7−15 nm), which attests that the crystallinity in the coalesced domains is low. On basis of the TEM observation, the smearing of the cylinder form factor is ascribed to the occurrence of coalescence of PCL cylinders prior to the development of significant amount of crystallinity. It is noted that the domain coalescence revealed by TEM ($t \sim 1.5$−3.5 h) occurs earlier than that observed by SAXS ($t \sim 4$−5.5 h) because crystallization may take place more rapidly in the ultrathin section than in the bulk.[22]

To further verify that the domain coalescence is responsible for the first stage of the perturbation of SAXS profiles (i.e., smearing of the cylinder form factor), we calculate the average surface-to-volume ratios (*S*/*V*) of the PCL domains from the three-dimensional correlation function defined as[23]

$$\gamma_3(r) = \frac{\int_0^\infty I(q) q^2 \frac{\sin(qr)}{qr} \, dq}{\int_0^\infty I(q) q^2 \, dq} \tag{4}$$

The correlation functions corresponding to some selected time frames are shown in Figure 9. Since the crystallinity is very low during the time period of 240−330 min, it is plausible to assume a two-phase model (i.e., amorphous PCL and PB phase) for the system. At small *r*, $\gamma_3(r)$ for such a two-phase model is given by

$$\gamma_3(r) = 1 - \frac{r}{l_p} \tag{5}$$

where l_p is the Porod length relating to *S*/*V* via

$$l_p = 4\frac{V}{S} f(1 - f) \tag{6}$$

where *f* is the volume fraction of one phase.

The inset of Figure 9 displays the calculated *S*/*V* as a function of crystallization time. It can be seen *S*/*V* experiences a sudden drop at $t \cong 240$ min, and it decreases progressively thereafter. The reduction of *S*/*V* is consistent with the occurrence of domain coalescence at the initial stage of crystallization.

The SAXS profiles are further used to calculate the normalized scattering invariants (*Q*) over the entire time frame via[21]

$$Q(t) = \frac{\int_0^\infty I(q) q^2 \, dq|_t}{\int_0^\infty I(q) q^2 \, dq|_{t\to\infty}} \tag{7}$$

The temporal variation of $Q(t)$ is shown in Figure 7 along with the crystallinity development. During the crystallization the system contains three types of domains, namely, PCL crystals (1), PCL amorphous domains (2), and PB amorphous domains (3). The invariant associated with this three-phase system can be calculated by[24]

$$Q = k(f_1 f_2 \Delta\rho_{12}{}^2 + f_2 f_3 \Delta\rho_{23}{}^2 + f_1 f_3 \Delta\rho_{13}{}^2) \tag{8}$$

where *k* is a constant scale factor and $\Delta\rho_{ij} = \rho_i - \rho_j$, the electron density contrast. The volume fractions of the three phases can be calculated from the PCL crystallinity assuming that the volume of the PB phase is conserved during PCL crystallization (i.e., the PB phase contains all the original h-PB chains mixed with PB blocks). The following values of the electron densities are adopted for the calculation of $\Delta\rho_{ij}$: $\rho_1 = 392.9$ e/nm^3 for crystalline PCL,[25] $\rho_2 = 350.3$ e/nm^3 for amorphous PCL,[26] and $\rho_3 = 291.7$ e/nm^3 for PB.[27] The value of *k* is chosen such that the invariant calculated using eq 8 reaches the ultimate value of 1.

The temporal variation of the invariant calculated by eq 8 is shown as the solid curve in Figure 7 for comparison with the observed invariant. It can be seen that the temporal variation of the calculated invariant closely follows that of the crystallinity. However, the observed invariants are larger than the calculated values between 270 and 390 min, while they match well with each other after 390 min. The time interval of 270−390 min corresponds well to the region where the coalescence of PCL cylinders with low crystallinity is observed. During this

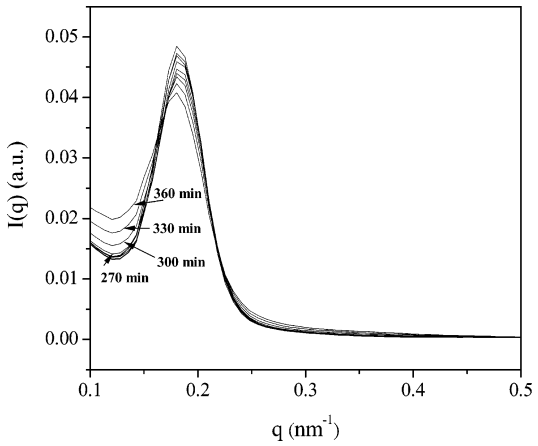

Figure 10. Time-resolved SAXS profiles of PCL-*b*-PB/h-PB with $f_{PB} = 0.78$ isothermally crystallized at 26 °C in linear scale. The profiles are displayed for every 60 min from 0 to 240 min and every 30 min from 240 to 360 min. The low-q intensity ($q < 0.16$ nm^{-1}) increases obviously from 270 to 360 min while the profiles match each other from 0 to 240 min.

time period, the increase of crystallinity is minor but the observed invariant increases apparently. A closer examination of the SAXS profiles during this time period reveals that the "excess" invariant is indeed contributed by the increase of intensity in the low-q region ($q < 0.16$ nm^{-1}), as shown in Figure 10. This means that an inhomogeneity with characteristic size larger than the interlamellsr distance develops at this early stage of crystallization.[28−30] This inhomogeneity is attributed to the h-PB domains situating between the lamellar stacks as revealed in Figure 4c. These h-PB domains create gaps in the lamellar stacking so as to contribute to an excess low-q scattering intensity.[28] Similar behavior has also been demonstrated for semicrystalline polymers[28] and crystalline/amorphous homopolymer blends.[29,30] In the present system, the domain coalescence causes the segregation of a fraction of h-PB chains out of the PB domains because the reduction of interfacial area allows less h-PB to be accommodated in the domains. As a result, a large-scale phase separation between h-PB and PB blocks takes place, leading to the formation of h-PB domains.

The domain coalescence at the early stage of crystallization may be driven by the deformation of microdomains due to the presence of PCL crystallites. The formation of lamellar crystallites within a fraction of PCL cylinders may deform their cross sections, and such a deformation increases the interfacial area and perturbs the conformation of the coronal PB blocks. The increase of free energy associated with these perturbations then triggers coalescence of the nearby cylinders. Once the coalescence is initiated, the PB block chains attached to the PCL microdomains neighboring to the coalesced domains may sense the difference between their conformation and the conformation of the PB blocks tethered to the coalesced domains; therefore, the coalescence propagates through this conformational communication to reduce the nonuniformity of conformational structure of PB blocks. However, after the first two cylinders fuse together, the distance between the fused microdomain and its nearby cylinders is increased by expelling h-PB into their gaps. As the coalescence further propagates, the distance between the coalesced domains and the cylinders further increases. There may be a limit where as the spacing becomes sufficiently large, the conformational communication can no longer pass on. As a result, the coalescence at the initial stage of crystallization only leads to the formation of rather isolated platelike microdomains instead of well-extended lamellae.

After crystallization inside the coalesced structure is completed, it requires another mechanism to induce the extended welding of the plate domains. We propose that this process is accomplished by drawing the PCL blocks from the molten domains to the crystal growth front in the coalesced domains. In this case, the PCL blocks may first dissociate from the PCL cylinders and diffuse to the growth front, leading to the development of extended lamellar stacks.[11,31]

Recently, several works have been devoted to the understanding of the crystallization-induced breakout in neat C−A diblock copolymers. Nojima et al.[11] and Hobbs and Register[31] have demonstrated that the breakout was initiated by dissociation of C blocks out of the microdomains followed by diffusing onto the crystal growth front. For the poly(ethylene-*co*-butylene)-*block*-poly(ethylene) system, Vasilev et al.[32] observed that the crystallization proceeded through a templated mechanism when the crystallinity (X_c) was lower than 20%; the breakout process then set in at the late stage where X_c lied above 20%. They attributed the templated crystallization in the initial stage to the incapability of the crystallization driving force to overcome the energy barrier imposed by the amorphous surrounding since the crystallinity was low. With increasing crystallinity, the perturbation of the mesophase became significantly pronounced to induce the breakout crystallization.

Our discussion on the mechanism of the breakout process may hence be summarized as follows. At the initial stage of crystallization, the tiny crystallites formed in the microdomains induce the deformation of PCL cylinders, which then drives a coalescence of the cylinders. The coalescence is transmitted by the conformational communication of the PB blocks. At the later stage, significant crystallization of PCL is accomplished by the diffusion of PCL from the molten microdomains to the growth front in the coalesced plates. An extended lamellar morphology eventually forms through this process.

Nonisothermal Crystallization Kinetics. Since the crystallization is not confined within the individual microdomains in the breakout crystallization, homogeneous nucleation to initiate the crystallizations in the predominant fraction of microdomains is no longer required.[6] In this case, the crystallization is able to proceed at relatively low undercooling through heterogeneous nucleation followed by long-range crystal growth. The corresponding Avrami exponent is usually larger than 1, which prescribes a sigmoidal shape of the crystallinity development during isothermal crystallization. For the system exhibiting confined crystallization, the isothermal crystallization in cylindrical and spherical morphology may follow the first-order kinetics prescribed by the homogeneous nucleation-controlled process. Furthermore, exceedingly large undercoolings are normally required to initiate the homogeneous nucleations in the majority of the microdomains.[33,34]

Previous works of the strongly segregated diblock systems showed that under a fixed cooling rate the freezing temperature (T_f) associated with the nonisothermal crystallization displayed a distinct correlation with the microdomain structure.[33−38] T_f dropped abruptly as the melt morphology changed from extended lamellae to dispersed cylinders. A second drop of T_f was observed as the morphology further transformed into spheres. Figure 11a shows the DSC cooling curves of PCL-*b*-PB/h-PB blends obtained at a fixed cooling rate of 5 °C/min. The peak temperature of the crystallization exotherm is defined as T_f, where a higher T_f corresponds to a faster crystallization rate. T_f is plotted as a function of f_{PB} in Figure 11b. It can be seen that, similar to the strongly segregated systems, the undercoolings required to initiate crystallizations in the cylindri-

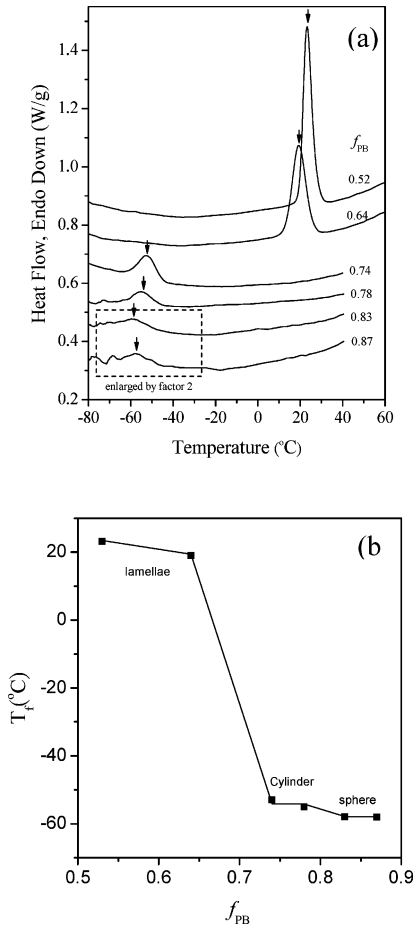

Figure 11. (a) DSC cooling curves of neat PCL-*b*-PB and PCL-*b*-PB/h-PB blends with a constant cooling rate of 5 °C/min. (b) A plot showing T_f as a function of f_{PB}. Three regimes corresponding to the three morphological patterns can be identified.

cal and spherical PCL domains are exceedingly large. As the blends containing cylindrical or spherical microdomains are cooled from the melt, the crystallizations tend to break out the melt mesophase to form lamellar morphology. However, this process is retarded by the presence of h-PB since it takes time to expel h-PB out of the coronal regions. As shown in the in-situ SAXS/WAXS results, the induction time required to initiate coalescence of the cylindrical microdomains in PCL-*b*-PB/h-PB with $f_{PB} = 0.78$ is 240 min at $T_c = 26$ °C, whereas it takes only around 27 min to cool the system from 85 to −50 °C. Once the breakout process cannot occur in time during the cooling, PCL blocks within most microdomains have to crystallize through the confined mode. Consequently, confined crystallization can be accessed by the nonisothermal crystallization at moderate cooling rate even for the relatively weakly segregated PCL-*b*-PB/h-PB blends.

Isothermal Crystallization Kinetics. The nonisothermal crystallization study shows that confined crystallization is still accessible in PCL-*b*-PB/h-PB blend because the presence of h-PB tends to resist the breakout process. Through the isothermal crystallization kinetics study, we intend to identify the temperature regions in which the breakout and confined crystallization become dominant for a cylinder-forming blend with $f_{PB} = 0.74$. The developments of relative crystallinity ($X_c(t)$) during the isothermal crystallizations of this blend at various temperatures are shown in the Supporting Information. It is noted that this composition is the one with the crystallization kinetics being detectable over a broad temperature range. The $X_c(t)$ curves were fitted by the classical Avrami equation, viz.

$$1 - X_c(t) = \exp(-kt^n) \tag{9}$$

where k is the temperature-dependent rate constant and n is the Avrami exponent depending on the crystallization mechanism. Table 1 lists the Avrami exponents along with the corresponding $t_{1/2}$ at different T_cs.

Figure 12 shows the reciprocal of $t_{1/2}$, which is proportional to the overall crystallization rate, as a function of T_c. The plot shows a typical bell shape above −40 °C. This temperature dependence of crystallization rate is due to the dominance of crystal growth rate given by[39,40]

$$G \propto \exp\left(-\frac{Q_D}{k_B(T_c - T_0)}\right)\exp\left(-\frac{4b_0\sigma\sigma_e T_m^0}{k_B T_c \Delta h_f^0 (T_m^0 - T_c)}\right) \tag{10}$$

where Q_D is the activation energy associated with the diffusion process in the crystallization, b_0 is the monomolecular thickness, σ and σ_e are the side and fold surface free energies, respectively, Δh_f^0 is the bulk enthalpy of melting per unit volume of crystal, T_m^0 is the equilibrium melting point, and T_0 is the temperature at which molecular diffusion is totally prohibited. The first exponential term in eq 10 is associated with the chain mobility whereas the second term is due to the secondary nucleation. The interplay between these two terms prescribes a bell shape for the T_c dependence of G.

Interestingly, an abrupt increase of crystallization rate is observed below −40 °C in Figure 12. This upturn is unexpected since at such a low temperature, the overall crystallization kinetics is still expected to be governed by the chain mobility if the crystallization rate is dominated by the crystal growth. Such an anomalous upturn may be attributed to the occurrence of homogeneous nucleation, which sets in at very large undercooling once the crystallization is largely confined. In homogeneous nucleation the nuclei with the critical dimension are formed by the random segmental aggregation through thermal fluctuations. Since such an event does not involve long-range chain diffusion as encountered in crystal growth, the nucleation rate is expressed by the following equation without considering the mobility term:[41]

$$i \propto \exp\left(-\frac{32\sigma^2\sigma_e T_m^{0\,2}}{(\Delta h_f^0)^2 k_B T_c (T_m^0 - T_c)^2}\right) \tag{11}$$

G and i are calculated as a function of T_c. The parameters used for the calculation, taken from the literature for PCL homopolymer, are listed in Table 2, and the calculated result is shown in Figure 13. The growth rate is found to show a maximum at 5 °C, which is about 15 °C higher than that found in Figure 12. Since eq 10 was developed for homopolymers, it may need to be modified for block copolymers by considering the extra diffusion barrier due to the junction constraint; consequently, the T_c at which the observed crystallization rate is maximum is different from that shown in Figure 13. The homogeneous nucleation rate is seen to exhibit a sudden rise near −40 °C. On basis of the result in Figure 13, the overall isothermal crystallization kinetics of the present system is considered to be largely controlled by the crystal growth at $T_c > -40$ °C because the crystallization can basically break out the melt structure, such that the overall crystallization process is analogous to that in the homopolymer, where the crystal growth can advance over a long range without involving a high nucleation density. At sufficiently low T_c the domain breakout is highly hindered due to sluggish mobility of PB; in this case, homo-

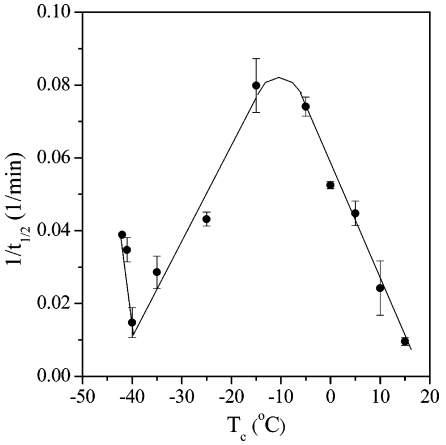

Figure 12. Inverse of $t_{1/2}$ as a function of T_c in a PCL-*b*-PB/h-PB with $f_{PB} = 0.74$. An upturn is clearly shown at T_c below −40 °C.

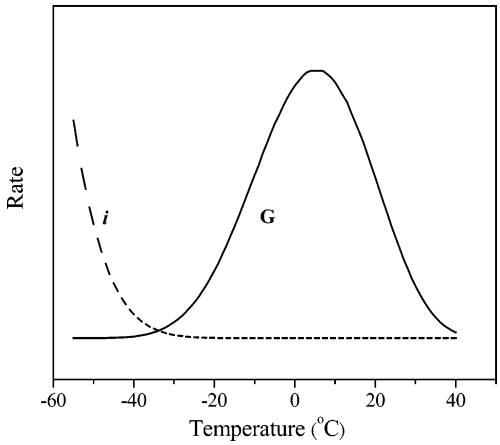

Figure 13. Calculated growth and homogeneous nucleation rates of PCL as a function of T_c. The parameters used for the calculations are listed in Table 2. The solid curve corresponds to the growth rate, and the dashed curve shows the homogeneous nucleation.

Table 1. Results of the Isothermal Crystallization Kinetics Analysis for a PCL-*b*-PB/h-PB with $f_{PB} = 0.74$ Crystallized at Different T_cs

T_c	Avrami exponent (n)	$t_{1/2}$ (min)	T_c	Avrami exponent (n)	$t_{1/2}$ (min)
15	2.6	94.3	−25	2.9	22.2
10	2.5	31.6	−35	2.0	41.4
5	2.2	19.7	−40	2.0	94.3
0	2.3	18.7	−41	1.6	26.3
−5	2.6	14.0	−42	1.6	25.7
−15	2.6	13.8			

Table 2. Parameters of PCL Used for the Calculations of Crystal Growth Rate and Homogeneous Nucleation Rate Using Eqs 10 and 11

parameters	values	source
Q_D (cal/mol)[a]	1500	ref 42
b_0 (cm)[b]	4.12×10^{-8}	ref 43
σ (erg/cm^2)	6.7	ref 44
σ_e (erg/cm^2)	87.1	ref 44
T_m^0 (°C)	74.7	ref 45
T_0 (°C)	−90	ref 44
Δh_f^0 (erg/cm^3)	1.63×10^9	ref 26

geneous nucleation greatly controls the crystallization kinetics, such that the crystallization rate exhibits a sudden increase.

Table 1 also reveals the effect of T_c on the Avrami exponent. At $T_c \geq -40$ °C the Avrami exponents exhibit the values (2−2.9) typical to that found in homopolymer crystallization, confirming that the crystallization is dominated by the breakout mode. The exponent drops to the value of 1.6 below −40 °C.

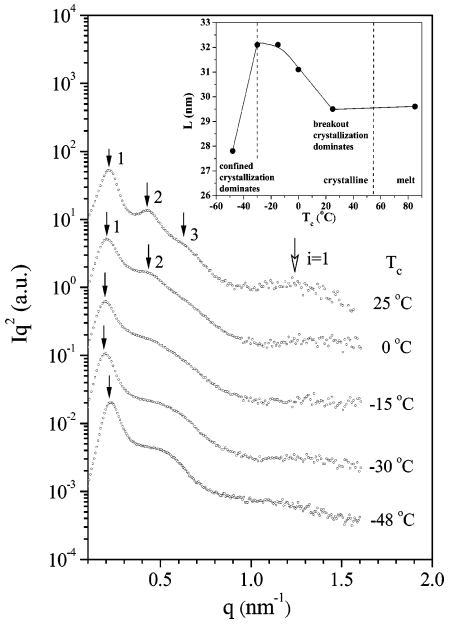

Figure 14. Lorentz-corrected SAXS profiles of PCL-*b*-PB/h-PB with $f_{PB} = 0.74$ crystallized at different T_cs for 4 h. The inset displays the interdomain distance L ($L = 2\pi/q_m$) as a function of T_c.

In this case, although the overall kinetics is governed by homogeneous nucleation, the crystallization process is still not completely controlled by the homogeneous nucleation which prescribes the Avrami index of 1.0[46,47] or less than 1.[48] Here the breakout of melt mesophase is prohibited; however, the interconnection of some cylindrical microdomains across the grain boundary may provide the percolation path which allows the crystal growth to advance over a relatively long distance.[49,50] As a result, the crystallization at very low temperatures may have proceeded through a "mixed mode", where both confined crystallization and percolation-assisted growth are operative. The coexistence of these two processes results in an average Avrami exponent of 1.6.

The hindrance of breakout at low T_c is further demonstrated by the SAXS profiles of the isothermally crystallized blend, as shown in Figure 14. As T_c decreases from 25 to −15 °C, the higher-order peaks relevant to lamellar morphology become obscured. At $T_c \leq -15$ °C, the higher-order lamellar peaks are replaced by a broad hump and the lamellar form factor peak is suppressed, implying a more complicated morphology which may consist of both crystalline lamellae and less perturbed or unperturbed microdomains. The broad hump may probably be associated with the spatial correlation between the crystallites contained within individual microdomains.[51] The inset of Figure 14 plots the interdomain distance L as a function of T_c. L is found to exhibit a sudden drop at $T_c \sim -48$ °C. This step change is proposed to be an indicative of significant suppression of morphological breakout when T_c is decreased to −48 °C. The isothermal crystallization kinetics study attests that the occurrence of homogeneous nucleation may lead to an anomalous acceleration of crystallization kinetics at sufficiently low T_c. Therefore, the crystallization behavior of PCL-*b*-PB/h-PB blend is more complicated than that of neat PCL-*b*-PB, since the crystallization process may break out the melt mesophases or largely confined within the individual microdomains depending upon T_c.

Conclusions

A symmetric PCL-*b*-PB was blended with an h-PB to form a series of PCL-*b*-PB/h-PB blends exhibiting lamellar, cylindri-

cal, and spherical morphologies in the melt. Upon crystallization at 26 °C, the blends were found to exhibit a lamellar morphology, where the PCL blocks underwent a breakout crystallization transforming the molten microdomains into extended lamellar stacks.

Time-resolved SAXS/WAXS experiments were conducted to reveal the mechanism of the breakout crystallization in the blend with $f_{PB} = 0.78$. The breakout crystallization was found to proceed through two stages. When the crystallinity was low, the crystallites situating in the cylindrical microdomains deformed the domains and caused coalescence of several PCL cylinders through conformational communication of PB blocks. The coalescence resulted in some PCL plates with limited length surrounded by the expelled h-PB chains and PB blocks. In the second step, the PCL blocks dissociated from the remaining cylindrical microdomains and diffused to the crystal growth front in the plates to generate well-extended crystalline lamellae.

In spite of the capability of the crystallization driving force to break out the melt mesophase, the crystallization of PCL in the cylindrical or spherical morphology may still be largely confined under the nonisothermal crystallization at 5 °C/min cooling rate and in the isothermal crystallizations at sufficiently low temperatures ($T_c < -40$ °C). The dominance of the confined crystallization led to an abrupt increase of overall crystallization rate below −40 °C for the blend with $f_{PB} = 0.74$. Further analysis of the temperature dependence of crystallization rate verified that the anomalous upturn was due to the dominance of homogeneous nucleation.

Acknowledgment. This work was supported by National Science Council of R.O.C. under Grant NSC 94-2216-E-007-002. The support by the National Synchrotron Radiation Research Center (NSRRC) for the time-resolved SAXS/WAXS experiments under project ID 2005-3-20-3 is also gratefully acknowledged.

Supporting Information Available: Table of parameters obtained from fits of SAXS profiles, table of enthalpies of crystallization and crystallinity of PCL-*b*-PB/h-PB blends, and figure of X_c vs time for PCL-*b*-PB/h-PB. This material is available free of charge via the Internet at http://pubs.acs.org.

References and Notes

(1) Leibler, L. *Macromolecules* **1980**, *13*, 1602.
(2) Hashimoto, T.; Shibayama, M.; Fujimura, M.; Kawai, H. In *Block Copolymers-Science and Technology*; Meier, D. J., Ed.; Harward Academic Publishers: London, 1983.
(3) Tanaka, H.; Hasegawa, H.; Hashimoto, T. *Macromolecules* **1991**, *24*, 240.
(4) Winey, K. I.; Thomas, E. L.; Fetters, L. J. *Macromolecules* **1992**, *25*, 2645.
(5) Hamley, I. W. *The Physics of Block Copolymers*; Oxford University Press: New York, 1998.
(6) Loo, Y.-L.; Register, R. A.; Ryan, A. J. *Macromolecules* **2002**, *35*, 2365.
(7) Xu, J.-T.; Fairclough, J. P. A.; Mai, S.-M.; Ryan, A. J.; Chaibundit, C. *Macromolecules* **2002**, *35*, 6937.
(8) Loo, Y.-L.; Register, R. A.; Ryan, A. J. *Phys. Rev. Lett.* **2000**, *84*, 4120.
(9) Nojima, S.; Kato, K.; Yamamoto, S.; Ashida, T. *Macromolecules* **1992**, *25*, 2237.
(10) Nojima, S.; Nakano, H.; Ashida, T. *Polymer* **1993**, *34*, 4168.
(11) Nojima, S.; Nakano, H.; Takahashi, Y.; Ashida, T. *Polymer* **1994**, *35*, 3479.
(12) Nojima, S.; Yamamoto, S.; Ashida, T. *Polym. J.* **1995**, *27*, 673.
(13) Hong, S.; Yang, L.; MacKnight, W. J.; Gido, S. P. *Macromolecules* **2001**, *34*, 7009.
(14) Zhu, L.; Cheng, S. Z. D.; Calhoun, B. H.; Ge, Q.; Quirk, R. P.; Thomas, E. L.; Hsiao, B. S.; Yeh, F.; Lotz, B. *Polymer* **2001**, *42*, 5829.
(15) Zhu, L.; Mimnaugh, B. R.; Ge, Q.; Quirk, R. P.; Cheng, S. Z. D.; Thomas, E. L.; Lotz, B.; Hsiao, B. S.; Yeh, F.; Liu, L. *Polymer* **2001**, *42*, 9121.
(16) Zhu, L.; Chen, Y.; Zhang, A.; Calhoun, B. H.; Chun, M.; Quirk, R. P.; Cheng, S. Z. D.; Hsiao, B. S.; Yeh, F.; Hashimoto, T. *Phys. Rev. B* **1999**, *60*, 10022.
(17) Nojima, S.; Tanaka, H.; Rohadi, A.; Sasaki, S. *Polymer* **1998**, *39*, 1727.
(18) Huang, Y.-Y.; Chen, H.-L.; Li, H.-C.; Lin, T.-L.; Lin, J. S. *Macromolecules* **2003**, *36*, 282.
(19) Huang, Y.-Y.; Yang, C. H.; Chen, H.-L.; Chiu, F.-C.; Lin, T.-L.; Liou, W. *Macromolecules* **2004**, *37*, 486.
(20) Hashimoto, T.; Fujimura, M.; Kawai, H. *Macromolecules* **1980**, *13*, 1660.
(21) Roe, R.-J. *Methods of X-Ray and Neutron Scattering in Polymer Science*; Oxiford University Press: New York, 2000; Chapter 5.
(22) Jukes, P. C.; Das, A.; Durell, M.; Trolley, D.; Higgins, A. M.; Geoghegan, M.; Macdonald, J. E.; Jones, R. A. L.; Brown, S.; Thompson, P. *Macromolecules* **2005**, *38*, 2315.
(23) Porod, G. In *Small Angle X-Ray Scattering*; Glatter, O., Kratky, O., Eds.; Academic Press: London, 1982; Chapter 2.
(24) Wang, Z.-G.; Phillips, R. A.; Hsiao, B. S. *J. Polym. Sci., Part B: Polym. Phys.* **2000**, *38*, 2580.
(25) Chatani, Y.; Okita, Y.; Tadokoro, H.; Yamashita, Y. *Polym. J.* **1970**, *1*, 555.
(26) Crescenzi, V.; Manzini, G.; Calzolari, G.; Borri, C. *Eur. Polym. J.* **1972**, *8*, 449.
(27) Rigby, D.; Roe, R.-J. *Macromolecules* **1986**, *19*, 721.
(28) Schultz, J. M. *J. Polym. Sci., Polym. Phys. Ed.* **1976**, *14*, 2291.
(29) Chen, H.-L.; Hsiao, M.-S. *Macromolecules* **1998**, *31*, 6579.
(30) Chen, H.-L.; Wang, S.-F. *Polymer* **2000**, *41*, 5157.
(31) Hobbs, J. K.; Register, R. A. *Macromolecules* **2006**, *39*, 703.
(32) Vasilev, C.; Reiter, G.; Pispas, S.; Hadjichristidis, N. *Polymer* **2006**, *47*, 330.
(33) Chen, H.-L.; Hsiao, S.-C.; Lin, T.-L.; Yamauchi, K.; Hasegawa, H.; Hashimoto, T. *Macromolecules* **2001**, *34*, 671.
(34) Chen, H.-L.; Wu, J.-C.; Lin, T.-L.; Lin, J. S. *Macromolecules* **2001**, *34*, 6936.
(35) Loo, Y.-L.; Register, R. A.; Ryan, A. J.; Dee, G. T. *Macromolecules* **2001**, *34*, 8968.
(36) Chen, H.-L.; Lin, S.-Y.; Huang, Y.-Y.; Chiu, F.-C.; Liou, W.; Lin, J. S. *Macromolecules* **2002**, *35*, 9434.
(37) Xu, J.-T.; Turner, S. C.; Fairclough, J. P. A.; Mai, S. M.; Ryan, A. J.; Chaibundit, C.; Booth, C. *Macromolecules* **2002**, *35*, 3614.
(38) Loo, Y.-L.; Register, R. A. In *Developments in Block Copolymer Science and Technology*; Hamley, I. W., Ed.; Wiley: New York, 2004; Chapter 6.
(39) Hoffman, J. D. *Polymer* **1983**, *24*, 3.
(40) Hoffman, J. D. *Polymer* **1982**, *23*, 656.
(41) Schultz, J. M. *Polymer Materials Science*; Prentice Hall: Englewood Cliffs, NJ, 1974.
(42) Hoffman, J. D.; Davis, G. T.; Lauritzen, J. I., Jr. In *Treatise on Solid State Chemistry*; Hannay, N. B., Ed.; Plenum Press: New York, 1976; Vol. 3.
(43) Bittiger, H.; Marchessault, R. H.; Niegisch, W. D. *Acta Crystallogr.* **1970**, *B26*, 1923.
(44) Phillips, P. J.; Rensch, G. J.; Taylor, K. D. *J. Polym. Sci., Part B: Polym. Phys.* **1987**, *25*, 1725.
(45) Chen, H.-L.; Li, L.-J.; Ou-Yang, W.-C.; Hwang, J. C.; Wong, W.-Y. *Macromolecules* **1997**, *30*, 1718.
(46) Turnbull, D.; Cormia, R. L. *J. Chem. Phys.* **1961**, *34*, 820.
(47) Cormia, R. L.; Price, F. P.; Turnbull, D. *J. Chem. Phys.* **1962**, *37*, 1333.
(48) Balsamo, V.; Urdaneta, N.; Pérez, L.; Carrizales, P.; Abetz, V.; Müller, A. J. *Eur. Polym. J.* **2004**, *40*, 1033.
(49) Müller, A. J.; Balsamo, V.; Arnal, M. L. *Adv. Polym. Sci.* **2005**, *190*, 1.
(50) Müller, A. J.; Balsamo, V.; Arnal, M. L.; Jakob, T.; Schmalz, H.; Abetz, V. *Macromolecules* **2002**, *35*, 3048.
(51) Loo, Y.-L.; Register, R. A.; Adamson, D. H. *Macromolecules* **2000**, *33*, 8361.

MA070369+